LANGMUIR

pubs.acs.org/Langmuir Article

Nanoscale Meniscus Dynamics in Evaporating Thin Films: Insights from Molecular Dynamics Simulations

Mustafa Ozsipahi* and Ali Beskok

Cite This: *Langmuir* 2023, 39, 18499−18508 Read Online

ACCESS | Metrics & More | Article Recommendations | Supporting Information

ABSTRACT: Evaporation studies are focused on unraveling heat transfer and flow dynamics near the solid−liquid−vapor contact line, particularly focusing on the meniscus, which encompasses the nonevaporating adsorbed layer, thin-film, and bulk meniscus regions. Continuum models assume that there are no evaporating adsorbed layers due to the strong intermolecular forces. However, recent molecular dynamics (MD) simulations have unveiled the significant role of adsorbed layers in thin-film evaporation. Leveraging a recently published energy-based interface detection method, the current study presents nonequilibrium MD simulation results for thin-film evaporation from a phase-change-driven nanopump using liquid argon confined between parallel platinum plates. Notably, unlike the transient simulations often encountered in the literature, the simulation system achieves a statistically steady transport. In this context, we showcase the shapes of the evaporating menisci for two distinct channel heights, 8 and 16 nm, and elucidate the underlying flow physics through velocity vectors and temperature contours. This comprehensive investigation advances our understanding of thin-film evaporation and its mechanisms, offering insights that span from nanoscale phenomena to broader thermal management applications.

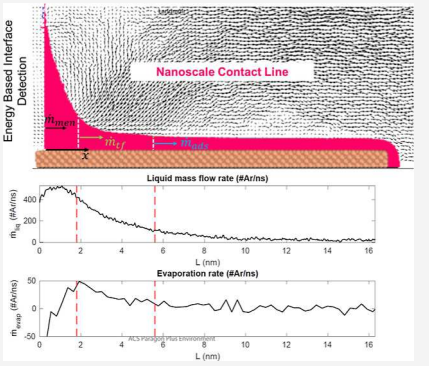

INTRODUCTION

Thin-film (tf) evaporation plays a critical role in diverse systems, including semiconductor fabrication, solar cells, energy storage, and thermal management.[1−5] tf evaporation, a form of phase-change cooling, utilizes latent heat energy through phase transition, providing efficient thermal management characterized by high heat evaporation fluxes ($O\approx 1$ kW/cm^2), uniform cooling, self-regulation, and high energy efficiency.[6−8]

Evaporation through tfs mostly occurs within the context of an evaporating meniscus. A meniscus refers to a curved liquid−vapor interface at the edge of a confined space, as illustrated in Figure 1. For simplicity, evaporating meniscus can be hypothetically divided into three subregions, particularly in the case of wetting fluids.[9−14] The first region is the adsorbed layer region, where the solid−liquid−vapor trijunction forms, creating an interface with nearly uniform thickness. The second subregion is the tf region, which connects the meniscus to the adsorbed film. This region yields varying radii of curvature (R) of the interface. The third subregion is the bulk fluid or meniscus region, where the R of the interface remains nearly constant. The adsorbed layer is characterized by its nearly uniform thickness and is assumed to be nonevaporating due to the significant disjoining pressure resulting from atomic interactions between the solid and liquid phases.[15−17] The macroscopic schematics of the evaporating meniscus are given in Figure 1c.

Contrary to the common assumption of nonevaporating adsorbed layers, our prior molecular dynamics (MDs) works presented adsorbed film evaporation which was not reported before.[18,19] However, pinpointing the evaporating meniscus in microscale contexts presents a challenge, and the nanoscale depiction of the evaporating meniscus is even more intricate. The liquid−vapor interface is a region of nearly 2 nm in thickness, which is very close to the characteristic length of the simulation domain.[18,20] Defining the contact line using density-based interface detection models leads to varying adsorbed film thicknesses due to the arbitrarily chosen cutoff values, and density fluctuations near the wall impact the contact line shape.[19,21] To overcome this issue, we introduced an energy-based interface detection method that identifies the contact line and eliminates the need to use an arbitrary density cutoff value.[21] This novel approach, based on the energetics of the molecular system to define the interface, offers advantages over traditional density-based interface detection methods. The energy-based liquid−vapor interface detection method is based on the kinetics and potential energy of atoms within the system. Specifically, it identifies the liquid−vapor interface as the location where the average kinetic energy of the atoms exceeds the average potential energy imposed by their neighboring molecules. This methodology can adapt seamlessly to variations in the meniscus position

Received: September 20, 2023
Revised: November 15, 2023
Accepted: November 15, 2023
Published: December 4, 2023

https://doi.org/10.1021/acs.langmuir.3c02830
Langmuir 2023, 39, 18499−18508

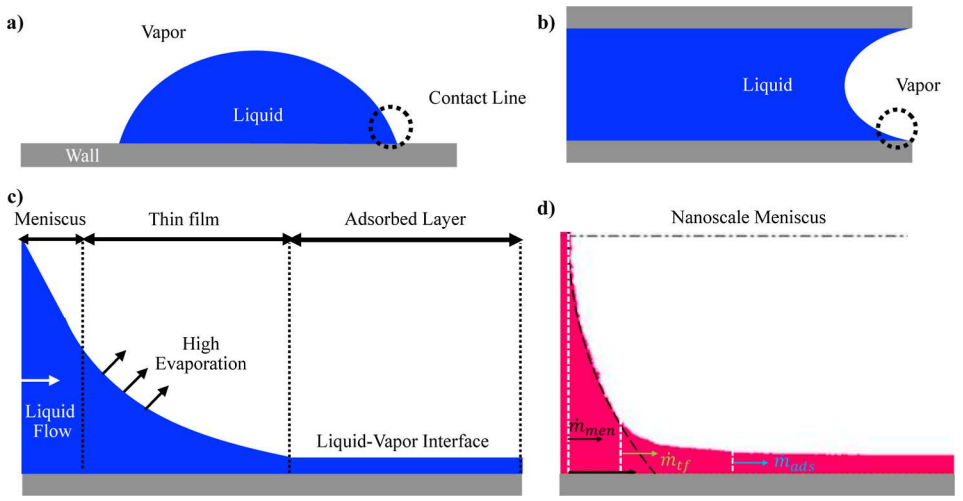

Figure 1. Classical schematics of evaporating meniscus profiles. Evaporation from (a) droplet and (b) capillary. (c) Classical microscale description of the evaporating meniscus can be segmented into three multiscale regions based on liquid film thickness and curvature. (d) Nanoscale evaporating meniscus profile. These nanoscale profiles were generated using the energy-based interface detection method, allowing the identification of distinct subregions within the evaporating meniscus. These regions include the adsorbed layer (ads), tf, and bulk meniscus (men) and are obtained from MD simulations.

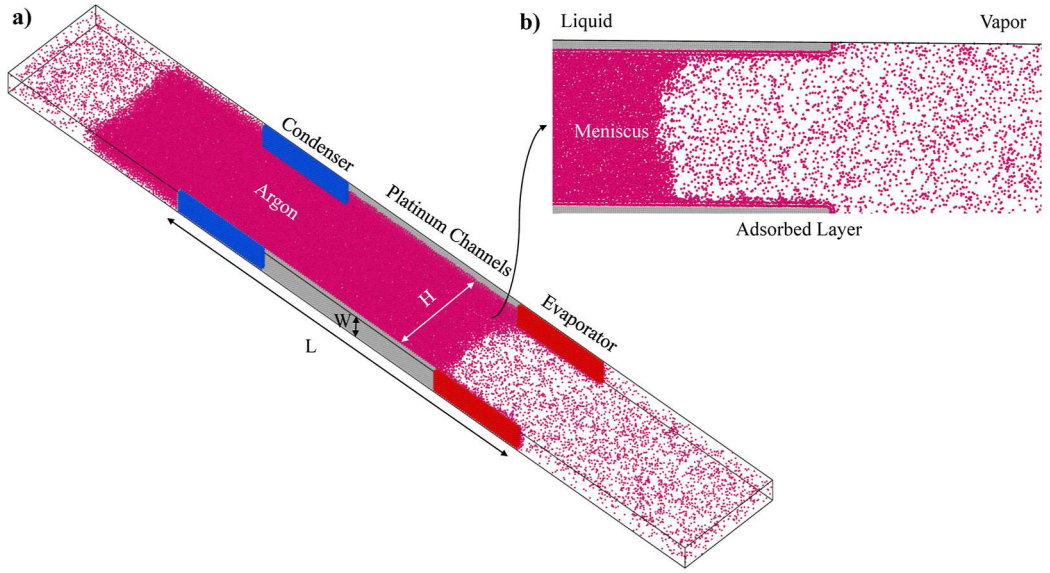

Figure 2. (a) Atomistic view of the NEMD simulation box of the 16 nm case. Gray color represents the Pt walls, while the magenta denotes the Ar atoms. On the right side of the walls, the sections colored in red indicate areas where heat is added (evaporator), whereas the blue regions represent zones for heat subtraction (condenser). The snapshot is taken at 160 ns, after the evaporating meniscus transitioned from the pinned to the receding region and reached a steady state. (b) Zoom in to instantaneous atomistic view of the evaporator section's frontal view. The liquid is pumping from the left (condenser) to the right (evaporator), facilitated by phase-change-driven pumping through the formation of an evaporating meniscus within the evaporator section. The evaporating meniscus itself, along with the adsorbed layer, is distinctly observable through the instantaneous atomic positions.

relative to the confining walls, ensuring an accurate representation of liquid adsorbed layers. Unlike conventional density cutoff methods commonly found in the literature, this new approach avoids the density layering effects that can disrupt the accuracy of interface detection, particularly in the vicinity of wall atoms in nanoconfinements. This new method yields much smoother evaporating meniscus profiles, even in close proximity to the wall regions, as seen in Figure 1d. Using this method, we investigated the impact of surface wettability on the evaporating meniscus and demonstrated self-regulation of the evaporating meniscus under diverse applied heat flux conditions and have shown that the evaporation from the adsorbed layer can account for up to 80% of the total evaporating mass in nanoscale systems.[18]

Identifying subregions of the evaporating meniscus within ultrasmall confinements is a difficult task.[22] The height of the channel becomes the constraining factor influencing the size of the meniscus within the confinement. This paper aims to investigate the size effects on the evaporating meniscus profiles, characterize the evaporating meniscus regions, and analyze tf evaporation characteristics in 8 and 16 nm height channels. We systematically increased the channel dimension to reveal evaporating meniscus regimes, identified adsorbed-layer, tf, and meniscus regions, and reported the axial mass flow rate of the subregions of the meniscus. Employing control volume analyses, we calculated the corresponding evaporation contributions. Additionally, we present the velocity vectors and

https://doi.org/10.1021/acs.langmuir.3c02830
Langmuir 2023, 39, 18499−18508

temperature contours to provide insights into this complex process. We anticipate that these findings will enhance the state of the art in understanding of tf evaporation,[23] offering insights that span from nanoscale phenomena to broader thermal management applications.

METHODOLOGY

MD simulations play a crucial role in modeling transport at the nanoscale, especially when direct point-wise measurements are limited. By providing a detailed view of the evaporation mechanisms and interactions between adsorbed, tf, and meniscus regions, MD is a crucial tool for probing interfacial heat transfer behavior at the nano- or subnanoscale.[24−27]

We conducted three-dimensional (3D) MD simulations to investigate the argon flow driven by the phase change between two parallel platinum plates, which were positioned at a separation distance of 7.84 nm. The simulation domain was defined with dimensions of 62.72 nm in the lateral direction, 9.21 nm in the vertical direction, and 3.92 nm in the longitudinal direction. To investigate the size effects, we increased both the lateral and vertical dimensions of the channel by *a* factor of 2 while keeping the longitudinal dimension constant. This resulted in a channel height of 15.68 nm and overall dimensions of 125.4 nm in the lateral, 17.05 nm in the vertical, and 3.92 nm in the longitudinal directions. For simplicity purposes, we refer to these two cases as 8 and 16 nm cases, respectively. Figure 2 depicts a 3D view of the simulation box and a frontal view of the evaporator section for the 16 nm case. In the visualization, argon atoms are illustrated in magenta, while platinum atoms are depicted in gray. Notably, the platinum walls exhibit regions highlighted in blue and red, which, respectively, represent areas of heat subtraction and addition. These designated regions have been termed the "condenser" and the "evaporator". The evaporator and condenser zones each correspond to 1/4th of the total channel length on each side, resulting in 7.84 and 15.6 nm for the 8 and 16 nm cases, respectively. The Large-scale atomic/molecular massively parallel simulator is used as the MD solver.[28] Periodicity boundary conditions are applied in three directions. The nanochannel comprises 4 layers of Pt molecules and possesses a face-centered cubic structure, employing a lattice constant of 3.92 Å. The (1, 0, 0) plane of the wall is oriented toward the fluid, and the outermost wall atoms are fixed in their original lattice location, resulting in a constant simulation domain volume. The embedded-atom method is employed for the interatomic forces of Pt atoms.[29] The interactions involving fluid−fluid and fluid−wall molecules are represented through the truncated Lennard-Jones (LJ) 12−6 potential given in the equation below

$$V_{\mathrm{trnc}}(r_{ij}) = 4\epsilon\left[\left(\frac{\sigma}{r_{ij}}\right)^{12} - \left(\frac{\sigma}{r_{ij}}\right)^{6} - \left(\frac{\sigma}{r_{\mathrm{c}}}\right)^{12} - \left(\frac{\sigma}{r_{\mathrm{c}}}\right)^{6}\right] \quad (1)$$

where ϵ is the depth of the potential well, σ is the molecular diameter, and r is the molecular distance. We utilized $\sigma_{\mathrm{Ar}} = 0.34$ nm, $\sigma_{\mathrm{Pt}} = 0.27$ nm, $\sigma_{\mathrm{Ar-Pt}} = 0.3085$ nm, and $\epsilon_{\mathrm{Ar}} = 0.01042$ eV. For reducing the calculation time, the LJ interactions utilized a cutoff distance of $r_{\mathrm{c}} = 3\sigma_{\mathrm{Ar}}$. The selection of the argon−platinum interaction parameter, $\varepsilon_{\mathrm{Ar-Pt}}$, is directly related to the wettability of the surface. In our previous work,[18] we explored the influence of surface wettability on tf evaporation, initially setting $\varepsilon_{\mathrm{Ar-Pt}}$ at 0.0055798 eV. Subsequently, we increased this parameter three and five times to investigate its impact on tf evaporation. These adjustments resulted in highly hydrophilic surfaces, known for their extended meniscus behavior. In this study, we selected $\varepsilon_{\mathrm{Ar-Pt}} = 0.0167394$ eV, resulting in a macroscopic contact angle of 27.47°, as determined from droplet studies. This selection was based on its ability to extend the meniscus into the channels, enabling a comprehensive observation of the adsorbed layer.

Simulations started using the Maxwell−Boltzmann velocity distribution for all molecules at 110 K. Newton's equation of motion for each atom is integrated with 5 fs time steps by using the Verlet algorithm. The system was relaxed using the canonical ensemble (*NVT*) (i.e., constant number of atoms *N*, volume *V*, and temperature *T*) for 10 ns to reach an isothermal state using the Nosé−Hoover thermostat. This is continued by applying the microcanonical ensemble (*NVE*) (i.e., constant number of atoms *N*, volume *V*, and energy *E*) on Ar atoms for another 10 ns while keeping the solid atoms at 110 K using the thermostat. To fix the thermodynamic state for all simulations, the numbers of vapor and liquid atoms were calculated by posteriori simulations and the total number of argon atoms is precisely reiterated to have the quality factor of $x \approx 0.05$ and two identical evaporating menisci are pinned at the entrance of the nanochannel tips (pinned region) at the end of this stage. A total of 76,908 Ar atoms and 25,680 Pt atoms are used for the 16 nm height case, while 18,850 Ar atoms and 12,880 Pt atoms are used for the 8 nm case. The average temperature of argon, the condenser, and the evaporator regions is monitored to ensure that the evaporating meniscus reaches a steady state. During the nonequilibrium MD (NEMD) simulation, the evaporation meniscus dynamically recedes into the nanochannel and extends and reveals the adsorbed layer along the evaporator section. The total simulation time carried out during the NEMD stage is 160 and 60 ns for the 16 and 8 nm cases, respectively.

In the third stage, we performed NEMD simulations by applying equal-energy addition and extraction to the evaporator and condenser zones of the channel, respectively. 10 and 13 nW heating/cooling rates are applied for the 8 and 16 nm cases, respectively. The calculated heat flux values at the channel walls in our study are 16.26 and 10.57 kW/cm^2 for the respective channel heights. These heat flux values are close to what is commonly observed in tf evaporation studies.[30,31] In order to avoid axial heat conduction through the walls, Pt atoms between the condenser and evaporator regions of the nanochannel were fixed in their positions (i.e., thermally frozen), but they were allowed to have atomistic interactions with neighboring Ar atoms. The average temperature of argon, the condenser, and the evaporator regions is monitored to ensure that the evaporating meniscus reaches a steady state. During the NEMD simulation, the evaporation meniscus dynamically recedes into the nanochannel and extends and reveals the adsorbed layer along the evaporator section. The total simulation time carried out during the NEMD stage is 160 and 60 ns for the 16 and 8 nm cases, respectively.

The data are processed using square bins with $\Delta x = 0.0392$ nm across the entire domain. The 16 nm height channel is divided in half, focusing on the evaporator section, using a similar binning approach. In both cases, a grid comprising 688,000 bins for the larger channel and 368,000 bins for the smaller channel is employed to discretize the domain. Wall temperature was obtained using rectangular bins with $\Delta x = 0.392$ nm and $\Delta y = 0.492$ nm for the evaporator and condenser regions. One million independent samples are collected for the 8 nm case, and 2 million independent samples are collected for the 16 nm case using the last 20 ns of NEMD simulations. We

https://doi.org/10.1021/acs.langmuir.3c02830
Langmuir 2023, 39, 18499−18508

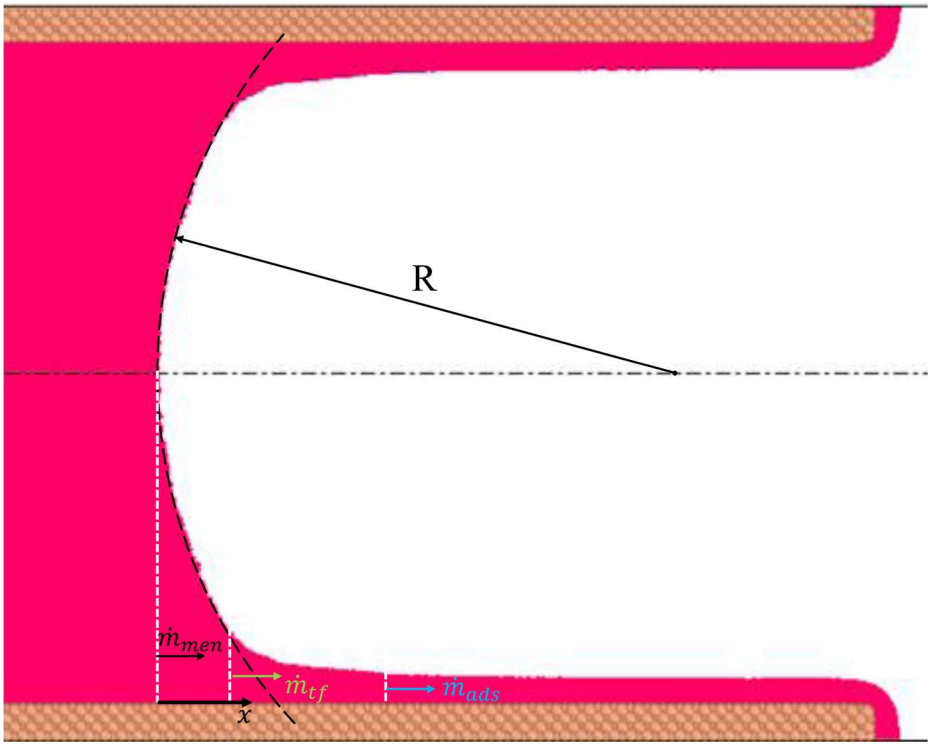

Figure 3. Evaporating meniscus profile of the 16 nm case. Evaporating meniscus is divided into three regions: meniscus, tf, and adsorbed layer. The circle is positioned precisely at the center of the evaporating meniscus, while the meniscus regions are identified by having a constant radius of curvature (R). tf region is from where R is no longer aligned with the interface to the start of the adsorbed layer, while the adsorbed layer is characterized by its nearly constant thickness (having less than 5% variation in its thickness).

increased the sample size 2-fold in the larger case to enhance the resolution in visualizing thermophysical properties. These samples are used to compute time-averaged temperature, density, kinetic and potential energy, and velocity distributions across the simulation domain.

RESULTS AND DISCUSSION

By utilizing the energy-based interface detection method,[21] the liquid−vapor interface of the evaporating meniscus is calculated for the 16 nm case, as shown in Figure 3. The magenta color corresponds to liquid argon, while the brown color represents the Pt walls. The dashed-dotted black line represents the channel center; white dashed vertical lines indicate the starting positions of the subregions of the meniscus. The axial distance is set to the 0 position on the x-axis, and it is aligned with the evaporating meniscus center.

The resulting liquid−vapor interface is nearly symmetrical for the bottom and top halves of the nanochannel. The smoothness of the liquid interface allows us to characterize the subregions of the evaporating meniscus. As previously mentioned, the size of the evaporating meniscus is on the same order as the channel height. Consequently, a channel height of 16 nm results in a broader profile for the adsorbed layer, resembling a microscale depiction of the evaporating meniscus.

The first region, the meniscus, is characterized by a constant radius of curvature denoted as R, which is fitted at the center of the evaporating meniscus. The dashed black line represents the fitted semicircle, aligning perfectly with the interface. The tf region starts from where the radius of curvature, R, deviates from the meniscus, and R changes through the tf until it meets with the adsorbed layer at the end. The tf region is characterized as being between the adsorbed layer and the meniscus region and corresponds to the highest mass flux along the interface. Within this specific zone, the liquid film thickness is relatively thin but introduces a moderate level of conduction resistance. Nonetheless, the film's thickness is adequately significant, resulting in a rapid decrease in interfacial resistance as the film thickness increases. These characteristics have been experimentally verified in studies[32,33] and replicated through numerical simulations by several investigators.[34−36] The adsorbed layer is identified by its thickness, which remains almost constant, varying by only 5% in thickness. The basis for selecting the 5% thickness change criterion is a direct result of energy-based interface detection in MD simulations. In traditional continuum models, it is often assumed that an adsorbed layer maintains a constant thickness without accounting for variations. However, our MD simulations revealed that there is indeed a change in thickness within the adsorbed layer. To accommodate this, we discretized the simulation domain into bins, approximately σ_{Ar}/7 in size, and calculated the change in thickness within the region spanning from 2 to 5 bins. This roughly corresponds to a thickness change of nearly 0.2 nm. While an alternative option to define the adsorbed-layer region is to use a cutoff based on disjoining pressure, it is important to recognize that the disjoining pressure is inversely proportional to the cube of the thickness of the adsorbed layer.[15]

After identifying the subregions of the evaporating meniscus, the next step is to calculate the mass flow rate to determine total contribution to the evaporation. The axial mass flow rate is calculated using the thickness of the liquid, the axial velocity (x), and the density. The details of its calculation are given in the Supporting Information. After the axial mass flow rate is calculated, control volume analyses of mass transport can explain how much fluid is evaporating within the corresponding

https://doi.org/10.1021/acs.langmuir.3c02830
Langmuir 2023, 39, 18499−18508

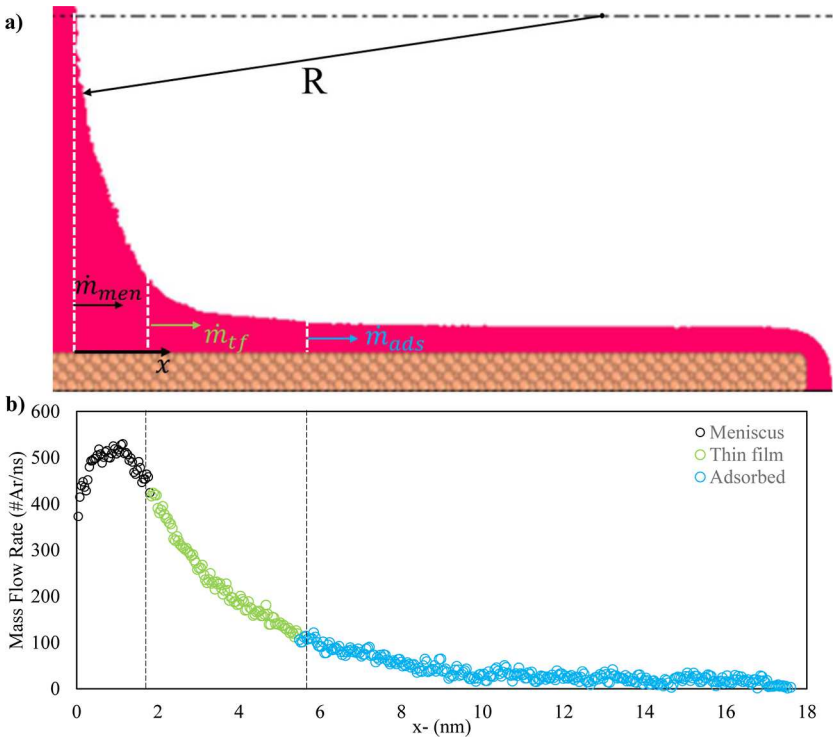

Figure 4. (a) Close-up view of the liquid−vapor interface and corresponding subregions of the menisci in the nanochannel confinement of the 16 nm case. (b) Axial mass flow rate of the evaporating meniscus. Black, green, and blue circles represent the meniscus, tf, and adsorbed-layer mass flow rates, respectively.

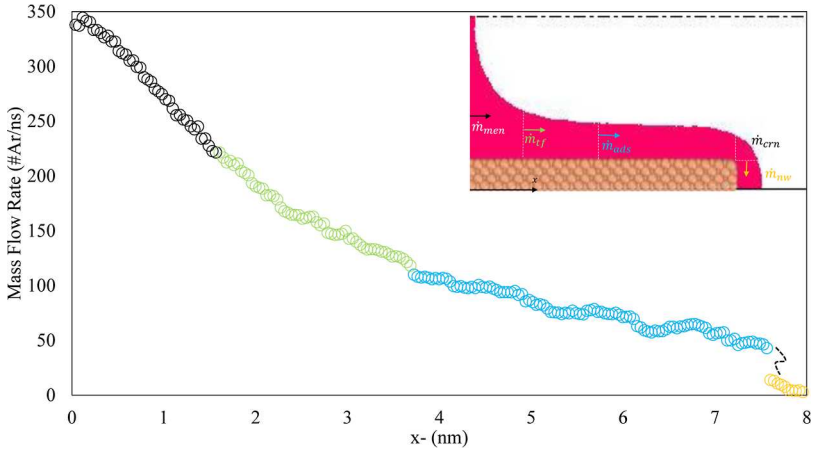

Figure 5. Meniscus, tf, and adsorbed-layer contributions to the total evaporation of the contact line in the 8 nm nanochannel. The liquid−vapor interface is presented at the inset. The origin (0 position) on the *x*-axis is precisely aligned with the center of the evaporating meniscus. The mass flow rate at the corner flow is depicted as a singular point, indicating a drop in the mass flow rate at that specific location. The region near the wall (nw) is highlighted in orange, illustrating the calculation of the mass flow rate near the wall within the extended meniscus.

section. In addition, total evaporating mass flow is equal to the channel mass flow rate by using the mass continuity equation. In this regard, the total mass flow rate is calculated at the channel center to quantify the total evaporating mass flow rate. Since the evaporating meniscus is nearly symmetrical at the top and bottom parts of the channel, only the bottom half is presented in the mass flow rate analyses.

Figure 4a presents the resulting liquid−vapor interface at the bottom part of the evaporator section. The axial mass flow rate of the subregions of the evaporating meniscus is given below, and dotted lines are plotted to guide the eye. Black, green, and blue colors represent the axial mass flow rate of the meniscus, tf, and adsorbed-layer regions, respectively. As seen in Figure 4b, most change in the axial mass flow rate occurs in the tf region (75%) and the meniscus region presents minimal evaporation (5%) according to the macroscopic picture. However, it is important to note that there is a significant mass flow rate contribution from the adsorbed-layer section, accounting for about 20% of the total. The primary evaporation predominantly occurs within the first 10 nm along the *x*-direction, beyond which it transitions to a nearly nonevaporative state, aligning with a macroscopic perspective, as shown in Figure 4b. We hypothesize that the mechanism driving the liquid flow inside the adsorbed layer is the thermal creep flow that occurs from cold toward hot zones, driven by the temperature gradient on the evaporator surface.[37] The axial mass flow rate in the adsorbed layer exhibited a

https://doi.org/10.1021/acs.langmuir.3c02830
Langmuir 2023, 39, 18499−18508

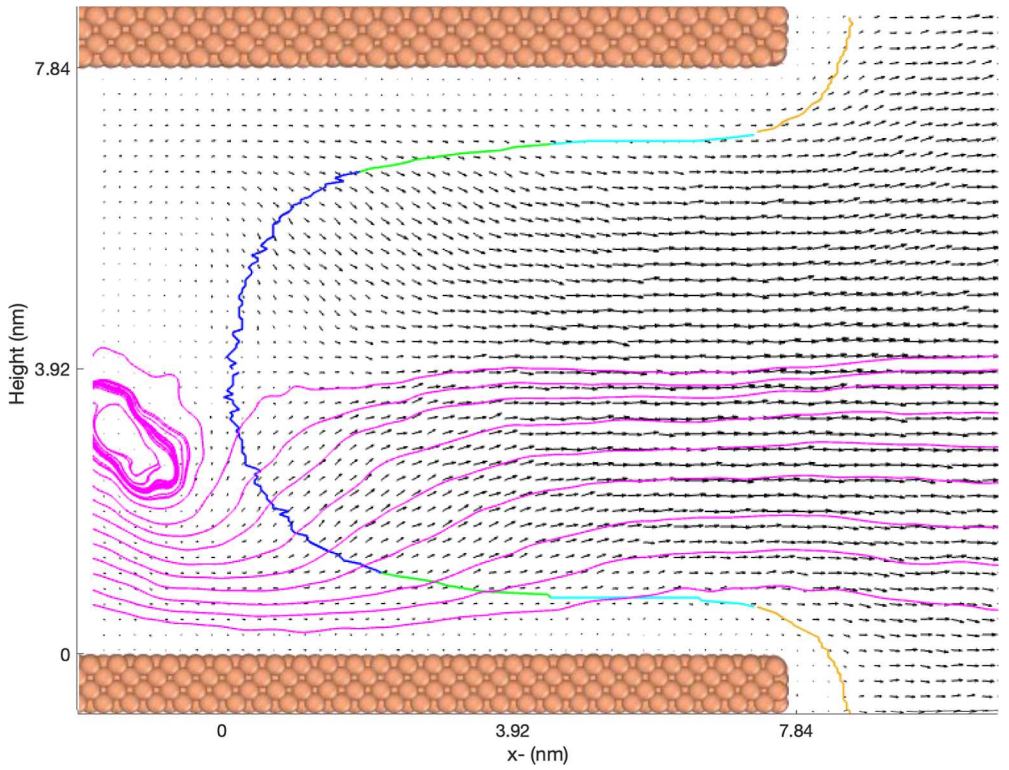

Figure 6. Velocity vectors and streamlines obtained from atomistic simulations and the evaporating interface profile of the 8 nm case. Color representation: blue (meniscus), green (tf), light blue (adsorbed-layer), and orange (near-wall) regions. Vertical and axial ticks represent *x*- and *y*-dimensions in nm. 0 position on the *x*-axis is aligned with the evaporating meniscus center. Magenta streamlines are plotted to reveal the flow path within the bottom half of the nanochannel.

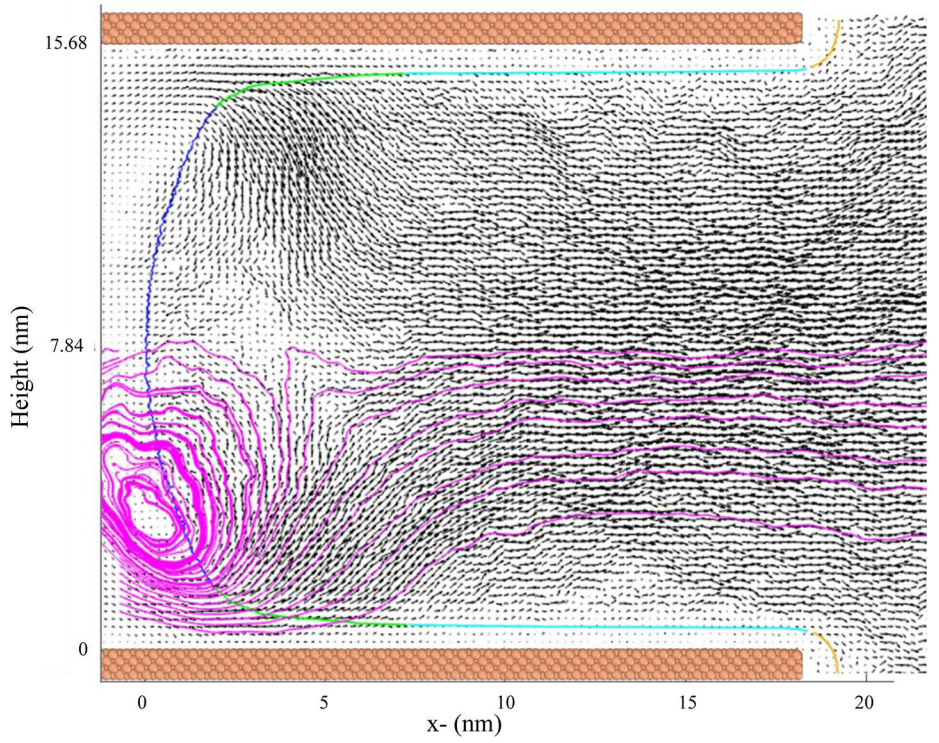

Figure 7. Velocity vectors and streamlines obtained from atomistic simulations and the evaporating interface profile of the 16 nm case. Color representation: blue (meniscus), green (tf), light blue (adsorbed-layer), and orange (near-wall) regions. Vertical and axial ticks represent *x*- and *y*-dimensions in nm. 0 position on the *x*-axis is aligned with the evaporating meniscus center. Magenta streamlines are plotted to reveal the flow path within the bottom half of the nanochannel.

https://doi.org/10.1021/acs.langmuir.3c02830
Langmuir 2023, 39, 18499−18508

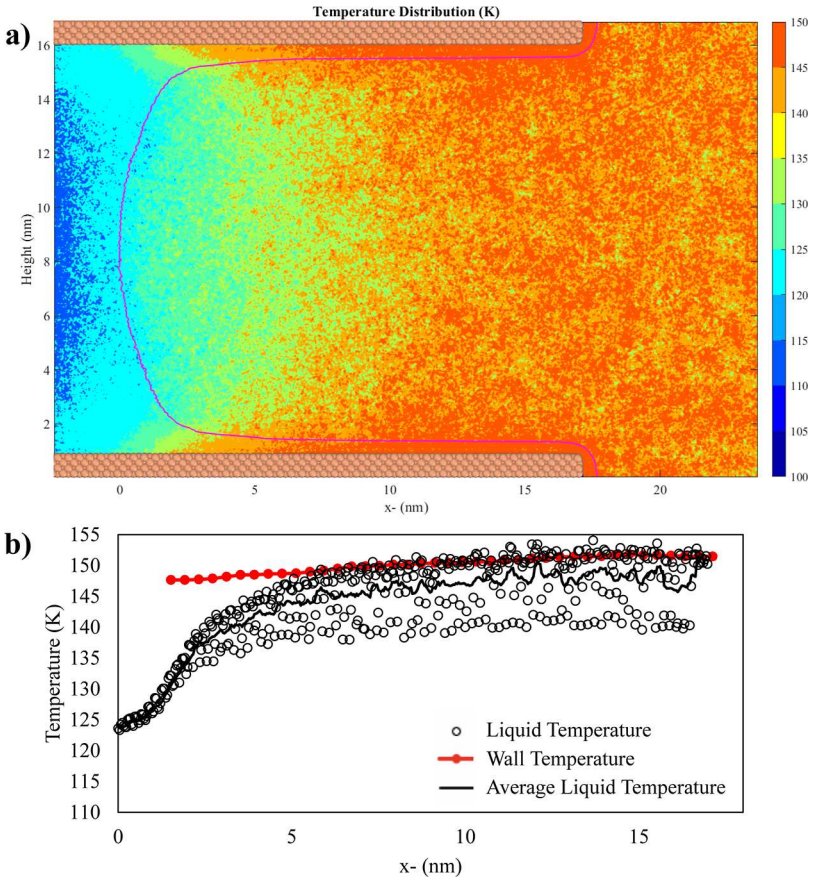

Figure 8. (a) Temperature contours and the profile of the evaporating meniscus of the 16 nm case. The contours are scaled from a minimum of 100 K to a maximum of 150 K. (b) Wall temperature (red) and liquid temperature (black circle) beneath the vapor−liquid interface. The average liquid temperatures (black line) are calculated by using a moving average over a five-period window.

significant contribution, particularly between 6 and 10 nm. Beyond this range, the mass flow rate remained relatively constant until the corner. We propose that temperature fluctuations within the adsorbed layer induce thermal creep, resulting in an observable mass flow rate, as depicted in Figure 4b. This effect is particularly pronounced within the 6−10 nm range, coinciding with a temperature increase of approximately 5 K within the adsorbed layer, as illustrated in Figure 8a. Beyond the 10 nm threshold, the mass flow rate becomes nearly stagnant and the temperature in the adsorbed layer approaches a steady state. The peak in the mass flow rate in the meniscus region is explained in the following sections.

Figure 5 presents the mass flow rate calculated with an 8 nm channel height. The liquid interface profile is provided as an inset for reference. Employing the methodology previously outlined, distinct regions within the system are identified: the meniscus, tf, and adsorbed layer. These regions are designated in a manner consistent with the explanation provided earlier. The distribution of mass flow rates among these regions is as follows: the meniscus region accounts for 35.2%, the tf region comprises 32.3%, and the adsorbed-layer region contributes 20.5% of the total mass flow rate. Furthermore, a noteworthy observation emerges concerning the corner flow and near-wall phenomena, collectively constituting almost 12% of the entire mass flow rate. An interesting trend becomes apparent—the mass flow rate exhibits a gradual decrease as one moves from the meniscus toward the adsorbed-layer region. This behavior is not only indicative of a distinct scenario in the 8 nm case but also aligns with our earlier findings obtained from the 4 nm cases, suggesting that evaporating meniscus regions are intertwined for channel dimensions less than 10 nm.

In order to gain a deeper understanding of the flow physics within the simulations, velocity vectors are investigated in the evaporator section for both cases. We grouped bins within the computational domain in sets of five to facilitate the calculation of average velocities which were then used to plot the velocity vectors across the simulation domain in Figures 6 and 7. In conjunction with these vectors, the liquid−vapor interface is highlighted to aid in the visual interpretation. Distinct regions are color-coded to represent various aspects: blue signifies the meniscus, green represents the tf, light blue corresponds to the adsorbed layer, and orange designates the near-wall regions. Although the vectors are derived from atomistic simulations, they effectively show significant flow structures adjacent to the interface. Remarkably symmetrical patterns emerge in the vector distribution across both the upper and lower halves of the evaporator section. The plotted velocity vectors reveal that the liquid phase exhibits a considerably lower magnitude compared to the vapor state due to its higher density. In contrast, gas atoms possess significantly higher speeds, resulting in markedly larger velocity magnitudes. In Figure 6, velocity vectors are depicted spanning the entire meniscus. Additionally, the streamlines are plotted and colored in magenta to reveal the flow structure in the evaporator section. The mass flow rate results, which clearly showed evaporation occurring in each of the subregions within the evaporating meniscus, are depicted in Figure 5. It is

https://doi.org/10.1021/acs.langmuir.3c02830
Langmuir 2023, 39, 18499−18508

presented through velocity vectors that each region within the evaporating meniscus contributes to the overall evaporation process. Furthermore, these distinct subregions are intricately interconnected, ultimately leading us to the conclusion that both the meniscus and the adsorbed layer play integral roles in the overall evaporation process. The circulation zone occurs just before the bulk meniscus and resulted in the flow turning through the meniscus. Along the evaporating meniscus, the adsorbed layer presents velocity vectors, resulting in tangential momentum and strong corner evaporation seen in the turning points on the wall side. It is also seen that there is no backflow through the meniscus from evaporating atoms from the tf regions.

When the channel size increases, the flow in the evaporation zone becomes more complex. The tf region, distinguished by its green color, displays a significant change in vector magnitude across the liquid−vapor interface, indicating active evaporation in this area. Additionally, gas atoms undergoing evaporation collide with each other near the center, resembling the collision of two high-speed streams. A considerable portion of these atoms is directed toward the channel exit, while a subset diverts back toward the meniscus, inducing a backflow of gas atoms that return to the meniscus region for condensation. As the channel height increases, the radius of curvature also expands, leading to a greater transmission angle for evaporating atoms in the tf region and a reduced probability of transmission of evaporating atoms within the capillary region. Furthermore, as shown in Figure 8a, the interface temperature decreases below the local gas temperature. These two effects collectively contribute to the localized condensation observed within the meniscus region.

The phase-change-induced pumping discussed in this study exhibits notable differences from the previously described thermal-gradient-driven mechanism in several aspects. First, prior reports of temperature gradients driving liquid argon showed much larger magnitudes, typically ranging from 12.5 to 81.2 K/nm.[38,39] In contrast, the phase-change mechanism in our study features a gradient of approximately 0.5 K/nm. Furthermore, our study encompasses all of the natural phenomena occurring during evaporation, including thermocapillarity, thermal creep, and advection. Thermocapillarity, characterized by variations in interface temperature, results in changes in surface tension along the interface, leading to a flow from the hot region to the cold region. Additionally, thermal transpiration, also known as thermal creep flow, occurs from the cold end to the hot end near the channel walls within the adsorbed layer. Moreover, advective flow, driven by phase change, generates a flow direction from the condenser to the evaporator for all studied nanochannel heights.[18,25] The circulation zones beneath the center of the meniscus are triggered by the interplay of thermocapillarity, thermal creep, and advective flow. Furthermore, the flow patterns within the meniscus region exhibit characteristics similar to Stokes flow, indicating that the meniscus itself significantly influences the flow, especially when navigating around corners, as depicted in Figure 7. The peak in the mass flow rate in Figure 4 is a result of the formation of a recirculation zone beneath the evaporating meniscus, directly caused by the change in the axial velocity direction.

Temperature contours are displayed in Figure 8a. As we move toward the evaporator section, the temperature increases due to heat being introduced to the walls. Examining the temperature at the liquid−vapor interface, initially the meniscus region registers temperatures around 120 K. A slight temperature increase is noted as we transition to the tf region, while a significant increase in temperature at the liquid interface becomes evident within this area. The interface temperature within the adsorbed layer remains nearly constant. The highest temperature is observed within the adsorbed layer region, and a substantial portion of the temperature variation is concentrated in the tf region.

The liquid and wall temperatures are presented in Figure 8b. The liquid temperature is computed from the center of the meniscus to the wall. The results reveal that the temperature increase predominantly takes place within the tf region. There is also a slight temperature increase observed as we approach the adsorbed layer, despite this region being the primary source of supplied heat flux. Within the adsorbed layer, where the thickness is merely 0.75 nm, roughly equivalent to two atomic diameters of argon, the liquid temperature experiences fluctuations. To mitigate this, a moving average with a five-point period is depicted as a black line. Conversely, the red line represents the wall temperature of the lower wall of the evaporator. Here, an increase of almost 5 K is observed as we shift from the inlet to the outlet of the nanochannel. The wall and the adsorbed-layer temperature can lead us to look at the kapitza resistance at the wall and adsorbed-layer interface. This can be done in the future and out of the context of this paper.

CONCLUSIONS

The presented study employs an energy-based interface detection method to accurately calculate the liquid−vapor interface of an evaporating meniscus within a nanochannel, focusing specifically on cases with channel heights of 16 and 8 nm. The resulting liquid−vapor interface exhibits a nearly symmetrical profile across the top and bottom halves of the nanochannel. This symmetrical behavior allows for the characterization of distinct subregions within the evaporating meniscus, namely, the meniscus, tf, and adsorbed layer. The meniscus region, positioned at the center of the evaporating meniscus, features a constant radius of curvature (R). Beyond this region, the tf begins where the radius of curvature deviates from that of R, and it extends to the start of the adsorbed layer. The adsorbed layer is marked by its nearly uniform thickness, varying by less than 5%. Within the tf region situated between the adsorbed layer and the meniscus, the highest mass flux along the interface is observed. This region's thickness remains relatively thin, introducing moderate conduction resistance. However, as the film thickness increases, the interfacial resistance decreases rapidly. These findings are consistent with those from prior experimental studies and numerical simulations.

The axial mass flow rates within each subregion are calculated, providing insights into the evaporation distribution. The tf region demonstrates the highest rate of change in axial mass flow, while the meniscus region displays minimal evaporation for the 16 nm case. Notably, the adsorbed layer contributes significantly to the total mass flow rate. In addition, an interesting trend emerges that sheds light on the behavior of the evaporating meniscus across different channel heights. The observation that the mass flow rate gradually decreases as one moves from the meniscus toward the adsorbed layer region not only is specific to the 8 nm case but also echoes our earlier findings from simulations involving 4 nm channel heights. This consistency across different channel dimensions suggests a common behavior in which the evaporating meniscus regions become intertwined when the channel height is less than 10 nm. In both cases, it is noteworthy that the adsorbed layer's

https://doi.org/10.1021/acs.langmuir.3c02830
Langmuir 2023, 39, 18499−18508

contribution to the total mass flow rate remains consistent at approximately 20%, highlighting its significance in the overall evaporation dynamics. This finding underscores the robustness of the observed phenomenon and its relevance across varying nanoscale geometries. Furthermore, the simulations reveal intricate flow patterns near the interface with gas atoms undergoing evaporation interacting and influencing backflows for the 16 nm case. Velocity vectors highlight symmetrical flow structures across the upper and lower halves of the evaporator section, while temperature contours illustrate temperature variations within different regions of the meniscus. In summary, the study elucidates the behavior of an evaporating meniscus within the nanochannel confinement, providing valuable insights into mass flow distribution, interface dynamics, and temperature variations. These findings contribute to a deeper understanding of fluid behavior at the nanoscale and hold implications for various applications involving evaporation and heat transfer.

■ ASSOCIATED CONTENT

Supporting Information

The Supporting Information is available free of charge at https://pubs.acs.org/doi/10.1021/acs.langmuir.3c02830.

Details of the calculation of the mass flow rate using control volume approach (PDF)

Transient response of the evaporating meniscus observed during the NEMD stage, spanning from 20 to 180 ns (MOV)

■ AUTHOR INFORMATION

Corresponding Author

Mustafa Ozsipahi − *U.S. DEVCOM Army Research Laboratory, Adelphi, Maryland 20783-1197, United States;* orcid.org/0000-0003-1378-3991; Email: mozsipahi@smu.edu

Author

Ali Beskok − *Southern Methodist University, Dallas, Texas 75205, United States;* orcid.org/0000-0002-8838-5683

Complete contact information is available at: https://pubs.acs.org/10.1021/acs.langmuir.3c02830

Author Contributions

M.O. performed MD simulations and wrote the manuscript. M.O and A.B. contributed to the conceptualization. A.B. reviewed and edited the manuscript.

Notes

The authors declare no competing financial interest.

■ ACKNOWLEDGMENTS

The material is based upon work by the National Science Foundation under grant no. CBET 2042239. Computations were carried out using the high-performance computing facilities of the Center for Scientific Computation at Southern Methodist University. It is our pleasure to thank Dr. Adam A. Wilson at U.S. Army Research Laboratory and Dr. Vladimir Ajaev from Southern Methodist University for their valuable comments on the paper.

■ REFERENCES

(1) Wayner, P., Jr; Kao, Y.; LaCroix, L. The interline heat-transfer coefficient of an evaporating wetting film. *Int. J. Heat Mass Transfer* **1976**, *19*, 487−492.

(2) Nahar, M. M.; Ma, B.; Guye, K.; Chau, Q. H.; Padilla, J.; Iyengar, M.; Agonafer, D. Review article: Microscale evaporative cooling technologies for high heat flux microelectronics devices: Background and recent advances. *Appl. Therm. Eng.* **2021**, *194*, 117109.

(3) Ma, H.; Cheng, P.; Borgmeyer, B.; Wang, Y. Fluid flow and heat transfer in the evaporating thin film region. *Microfluid. Nanofluidics* **2008**, *4*, 237−243.

(4) Jin, M.; Qu, X.; Li, J.; Deng, L.; Han, Z.; Chen, S.; Wang, H. Bacterial cellulose-based film with self-floating hierarchical porous structure for efficient solar-driven interfacial evaporation. *Carbohydr. Polym.* **2023**, *321*, 121324.

(5) Adera, S.; Antao, D.; Raj, R.; Wang, E. N. Design of micropillar wicks for thin-film evaporation. *Int. J. Heat Mass Transfer* **2016**, *101*, 280−294.

(6) Nazari, M.; Masoudi, A.; Jafari, P.; Irajizad, P.; Kashyap, V.; Ghasemi, H. Ultrahigh evaporative heat fluxes in nanoconfined geometries. *Langmuir* **2019**, *35*, 78−85.

(7) Li, Y.; Chen, H.; Xiao, S.; Alibakhshi, M. A.; Lo, C.-W.; Lu, M.-C.; Duan, C. Ultrafast diameter-dependent water evaporation from nanopores. *ACS Nano* **2019**, *13*, 3363−3372.

(8) Hanks, D. F.; Lu, Z.; Sircar, J.; Kinefuchi, I.; Bagnall, K. R.; Salamon, T. R.; Antao, D. S.; Barabadi, B.; Wang, E. N. High heat flux evaporation of low surface tension liquids from nanoporous membranes. *ACS Appl. Mater. Interfaces* **2020**, *12*, 7232−7238.

(9) Plawsky, J.; Fedorov, A.; Garimella, S.; Ma, H.; Maroo, S.; Chen, L.; Nam, Y. Nano-and microstructures for thin-film evaporation—A review. *Nanoscale Microscale Thermophys. Eng.* **2014**, *18*, 251−269.

(10) Ibrahem, K.; Abd Rabbo, M.; Gambaryan-Roisman, T.; Stephan, P. Experimental investigation of evaporative heat transfer characteristics at the 3-phase contact line. *Exp. Therm. Fluid Sci.* **2010**, *34*, 1036−1041.

(11) Lakew, E.; Sarchami, A.; Giustini, G.; Kim, H.; Bellur, K. Thin film evaporation modeling of the liquid microlayer region in a dewetting water bubble. *Fluids* **2023**, *8*, 126.

(12) Ajaev, V. S.; Kabov, O. A. Heat and mass transfer near contact lines on heated surfaces. *Int. J. Heat Mass Transfer* **2017**, *108*, 918−932.

(13) Wang, H.; Garimella, S. V.; Murthy, J. Y. Characteristics of an evaporating thin film in a microchannel. *Int. J. Heat Mass Transfer* **2007**, *50*, 3933−3942.

(14) Ma, B.; Guye, K.; Dogruoz, B.; Agonafer, D. Molecular dynamics simulations of thin-film evaporation: The influence of interfacial thermal resistance on a graphene-coated heated silicon substrate. *Appl. Therm. Eng.* **2021**, *195*, 117142.

(15) Ajaev, V. S. *Interfacial fluid mechanics*; Springer, 2012.

(16) Raghupathi, P. A.; Kandlikar, S. G. Contact line region heat transfer mechanisms for an evaporating interface. *Int. J. Heat Mass Transfer* **2016**, *95*, 296−306.

(17) Dwivedi, R.; Singh, P. K. Thin film evaporation: New insights with nanofluid inclusion and component of the electrostatic interactions. *Phys. Fluids* **2022**, *34*, 34.

(18) Ozsipahi, M.; Akkus, Y.; Beskok, A. Surface wettability effects on evaporating meniscus in nanochannels. *Int. Commun. Heat Mass Tran.* **2022**, *136*, 106166.

(19) Akkus, Y.; Koklu, A.; Beskok, A. Atomic scale interfacial transport at an extended evaporating meniscus. *Langmuir* **2019**, *35*, 4491−4497.

(20) Fan, J.; Wu, H.; Wang, F. Evaporation-driven liquid flow through nanochannels. *Phys. Fluids* **2020**, *32*, 32.

(21) Ozsipahi, M.; Akkus, Y.; Nguyen, C. T.; Beskok, A. Energy-Based Interface Detection for Phase Change Processes of Monatomic Fluids in Nanoconfinements. *J. Phys. Chem. Lett.* **2021**, *12*, 8397−8403.

(22) Sefiane, K.; Ward, C. A. Recent advances on thermocapillary flows and interfacial conditions during the evaporation of liquids. *Adv. Colloid Interface Sci.* **2007**, *134*−*135*, 201−223.

(23) Lu, Z.; Narayanan, S.; Wang, E. N. Modeling of evaporation from nanopores with nonequilibrium and nonlocal effects. *Langmuir* **2015**, *31*, 9817−9824.
(24) Yenigun, O.; Barisik, M. Active heat transfer enhancement by interface-localized liquid dielectrophoresis using interdigitated electrodes. *Carbon* **2022**, *189*, 339−348.
(25) Akkus, Y.; Beskok, A. Molecular diffusion replaces capillary pumping in phase-change-driven nanopumps. *Microfluid. Nanofluidics* **2019**, *23*, 14.
(26) Warzoha, R. J.; Wilson, A. A.; Donovan, B. F.; Donmezer, N.; Giri, A.; Hopkins, P. E.; Choi, S.; Pahinkar, D.; Shi, J.; Graham, S.; et al. Applications and Impacts of Nanoscale Thermal Transport in Electronics Packaging. *J. Electron. Packag.* **2021**, *143*, 020804.
(27) Donovan, B. F.; Warzoha, R. J.; Cosby, T.; Giri, A.; Wilson, A. A.; Borgdorff, A. J.; Vu, N. T.; Patterson, E. A.; Gorzkowski, E. P. Strained polymer thermal conductivity enhancement counteracted by additional off-axis strain. *Macromolecules* **2020**, *53*, 11089−11097.
(28) Thompson, A. P.; Aktulga, H. M.; Berger, R.; Bolintineanu, D. S.; Brown, W. M.; Crozier, P. S.; in 't Veld, P. J.; Kohlmeyer, A.; Moore, S. G.; Nguyen, T. D.; Shan, R.; Stevens, M. J.; Tranchida, J.; Trott, C.; Plimpton, S. J. LAMMPS - a flexible simulation tool for particle-based materials modeling at the atomic, meso, and continuum scales. *Comput. Phys. Commun.* **2022**, *271*, 108171.
(29) Daw, M. S.; Foiles, S. M.; Baskes, M. I. The embedded-atom method: a review of theory and applications. *Mater. Sci. Rep.* **1993**, *9*, 251−310.
(30) Adera, S.; Antao, D. S.; Raj, R.; Wang, E. N. Hotspot thermal management via thin-film evaporation—Part I: Experimental characterization. *IEEE Trans. Compon., Packag., Manuf. Technol.* **2018**, *8*, 88−98.
(31) Adera, S.; Antao, D. S.; Raj, R.; Wang, E. N. Hotspot thermal management via thin-film evaporation—part II: modeling. *IEEE Trans. Compon., Packag., Manuf. Technol.* **2018**, *8*, 99−112.
(32) Soma, S.; Kunugi, T. Theoretical scaling law for predicting evaporation rate from meniscus. *Int. J. Heat Mass Transfer* **2019**, *134*, 143−148.
(33) Hanchak, M.; Vangsness, M.; Byrd, L.; Ervin, J.; Jones, J. Profile measurements of thin liquid films using reflectometry. *Appl. Phys. Lett.* **2013**, *103*, 211607.
(34) Narayanan, S.; Fedorov, A. G.; Joshi, Y. K. Interfacial transport of evaporating water confined in nanopores. *Langmuir* **2011**, *27*, 10666−10676.
(35) Kolliopoulos, P.; Jochem, K. S.; Francis, L. F.; Kumar, S. Capillary flow of evaporating liquid solutions in open rectangular microchannels. *J. Fluid Mech.* **2022**, *938*, A22.
(36) Bellur, K.; Médici, E. F.; Choi, C. K.; Hermanson, J. C.; Allen, J. S. Multiscale approach to model steady meniscus evaporation in a wetting fluid. *Phys. Rev. Fluids* **2020**, *5*, 024001.
(37) Thekkethala, J. F.; Sathian, S. P. Thermal transpiration through single walled carbon nanotubes and graphene channels. *J. Chem. Phys.* **2013**, *139*, 174712.
(38) Liu, C.; Li, Z. Molecular dynamics simulation of composite nanochannels as nanopumps driven by symmetric temperature gradients. *Phys. Rev. Lett.* **2010**, *105*, 174501.
(39) Liu, C.; Lv, Y.; Li, Z. Fluid transport in nanochannels induced by temperature gradients. *J. Chem. Phys.* **2012**, *136*, 114506.

https://doi.org/10.1021/acs.langmuir.3c02830
Langmuir 2023, 39, 18499−18508